Journal of Geodesy (2022) 96:78
https://doi.org/10.1007/s00190-022-01666-1

ORIGINAL ARTICLE

3D-mapping-aided PPP-RTK aiming at deep urban canyons

Shaoming Xin[1,2] · Jianghui Geng[1,3] · Guohao Zhang[2] · Hoi-Fung Ng[2] · Jiang Guo[1] · Li-Ta Hsu[2]

Received: 26 May 2022 / Accepted: 4 September 2022 / Published online: 15 October 2022

Abstract

As a hot topic in the GNSS community in recent years, PPP-RTK integrates the advantages of PPP and RTK, aiming to quickly realize centimeter-level single point positioning with ambiguity resolution. However, PPP-RTK still faces challenges in difficult urban environments. The performance of precise positioning will seriously deteriorate by the receptions of complex multipath and NLOS (non-light-of-sight) signals. The 3D-mapping-aiding (3DMA) method has been proven effective in urban navigation and positioning, such as detecting and excluding NLOS satellites. But the rough excluding strategy may cause more insufficient satellites. Thus, this study proposes a 3D-mapping-aided weighting algorithm to enhance the performance of PPP-RTK in complex urban environments. We modeled the 3DMA weighting function first by analyzing static GNSS data in various urban environments. Then, the proposed algorithm was applied to both static and kinematic positioning experiments. According to the results, the 3DMA weighting can be complementary to the classic C/N_0 weighting: the 3DMA weighting can identify those poor measurements with high-C/N_0 in urban environments while the C/N_0 takes only a rough and preliminary diagnostic of the measurements. It could accelerate convergences and mitigate some outliers in slight and medium urban environments. In deep urban environments, it could achieve positioning availability of more than 90% with a horizontal precision of better than 20 cm, while the availability of traditional PPP-RTK without 3DMA may be less than 50%. The RMSs in horizontal components of the positioning errors after convergence are generally less than 10 cm while classic PPP-RTK reaches only the sub-meter level most of the time. We believe the 3DMA algorithm can benefit the precise GNSS positioning in urban canyons.

Keywords 3DMA · PPP-RTK · Weighting · Urban environments

1 Introduction

Urban precise positioning is increasingly attracting people's attention, since it can play an important role in many emerging areas, such as pedestrian navigation, autonomous driving and unmanned aerial vehicle distribution. As an absolute positioning mean, GNSS positioning is very crucial and necessary. Precise point positioning (PPP) and real-time kinematic (RTK) are two major GNSS precise positioning methods since the end of the twentieth century. With the help of precise satellite orbits and clocks, PPP can provide centimeter-level positioning solutions based on a single station (Zumberge et al. 1997). However, the performance of PPP is always affected by its slow convergence (e.g., a few tens of minutes typically for GPS). Even using the ambiguity resolution (AR) method and multi-GNSS multi-frequency GNSS data, the convergence still has to cost several minutes. Geng et al. (2020) studied that triple-frequency GPS/GALILEO/BDS-2/QZSS PPP-AR needs to spend 6 min on average to achieve convergence. For RTK, as a relative positioning technique, it needs at least one baseline to build double-differenced GNSS observations so that the common delays could be eliminated (Counselman and Gourevitch 1981). However, the performance of RTK depends on the quality of the reference station and the length of the baseline. A long baseline usually cannot eliminate distance-dependent biases (e.g., atmospheric delays), resulting in a less accurate result. The NRTK (Network RTK),

✉ Jianghui Geng
jgeng@whu.edu.cn

✉ Li-Ta Hsu
lt.hsu@polyu.edu.hk

1 GNSS Research Center, Wuhan University, Wuhan, China

2 Department of Aeronautical and Aviation Engineering, The Hong Kong Polytechnic University, Hung Hom, Hong Kong, China

3 Hubei Luojia Laboratory, Wuhan University, Wuhan, China

which is based on the continuously operating reference station network, can generate better virtual observations or corrections in observation space for rover stations to realize relative positioning (Rizos 2002). However, NRTK usually needs a dense station network. This technique is not only enduring the pressure from infrastructure building and costs, but also facing the burden from the observation space representation (OSR) mode and communication (Wübbena et al. 2005). In recent years, PPP-RTK becomes more and more popular in the GNSS community. The PPP-RTK technology integrates the superiorities of PPP and RTK (Wübbena et al. 2005). PPP-RTK can achieve convergences and ambiguity resolutions as fast as NRTK in general. In contrast to the OSR of NRTK, the state space representation (SSR) is adopted by PPP-RTK. The advantages of SSR are well-known, especially for marine applications, such as a small bandwidth, the uni-directional communication link and minimizing station-dependent GNSS errors (Wübbena et al. 2005). The detailed error analyses when studying the integrity and functional safety in many applications (e.g., autonomous driving) can also be achieved conveniently. Users can also receive the SSR corrections they need, such as using only the atmospheric product to analyze the atmosphere, and the information is accurate. PPP-RTK has both server and user ends. The SSR information generated by the server end is essential for PPP-RTK, including satellite phase biases, ionospheric corrections and tropospheric corrections (Wübbena et al. 2005; Teunissen et al. 2010; Geng et al. 2010, 2011; Zhang et al. 2011; Banville et al. 2014; Odijk et al. 2016; Wu et al. 2020). Considering the ease of the communication budget, PPP-RTK is a promising technique in urban areas.

In an open-sky environment, GNSS PPP-RTK can quickly realize centimeter-level single point positioning with ambiguity resolution (e.g., instantaneous centimeter-level positioning) (Odijk et al. 2016; Zhang et al. 2019; Psychas and Verhagen 2020; Wu et al. 2020). However, we cannot ignore the vulnerability of GNSS signals. Multipath effects and none-light-of-sight (NLOS) receptions are the two main challenges for GNSS positioning in the urban canyon (Groves et al. 2013). This intrinsic characteristic of a GNSS receiver can easily be affected by the two notorious effects in the urban canyon, resulting in large biases and highly noisy pseudorange and carrier-phase measurements. This will degrade the performance of PPP-RTK. Thus, how to handle the unsatisfactory GNSS measurements is a crucial issue for urban GNSS positioning. Mitigating the multipath is a common approach to improving positioning precision. The sidereal filtering and the multipath hemispherical map (Ragheb et al. 2007; Dong et al. 2016) are two kinds of classic methods in the geodesy community, but they are only suitable for (quasi-)static stations. As for urban environments, the approaches of detecting and excluding or de-weighting the multipath-affected measurements are popular. Based on the raw GNSS measurements, C/N_0 (carrier-to-noise-density ratio) has been widely used. Realini and Reguzzoni (2013) proposed a sophisticated C/N_0 based weighting algorithm that significantly improves the precision by about 20%. Jiang and Groves (2014) used C/N_0 to detect NLOS signals with a dual-polarization antenna. However, Hsu (2018) indicated that the received signal strength is not the only factor to correlate with the NLOS delay in deep urban canyons.

The 3D building model has been widely studied and adopted for the applications of urban navigation (e.g., van Diggelen 2021). It becomes a digital infrastructure, which can facilitate GNSS users with connectivity such as intelligent vehicles and smartphone users. Generally, there are two typical approaches to using the 3D building model for intelligent urban navigation. One is GNSS shadow matching which is based on the satellite visibility and 3D building model (Groves 2011; Groves et al. 2015). It can effectively determine which side of the user standing on. However, it struggles with low accuracy in the along-street direction (Groves et al. 2015). The other one is based on GNSS ray-tracing (Lau and Cross 2007), realizing positioning by comparing the ray-tracing simulated and observed observations (Suzuki and Kubo 2013; Miura et al. 2015; Hsu et al. 2016). Ray-tracing can calculate the reflection delays and provide corrections by predicting the signal path. Zhong and Groves (2021) also used the likelihood-based 3DMA GNSS via a statistical model to correct the pseudorange effectively. Besides, many other studies usually use the 3D building model to assist classic GNSS positioning, such as excluding the measurements with multipath or NLOS effects, modeling NLOS effects by 3D-mapping-derived indexes, etc. (Groves et al. 2012; Ahmad et al. 2013; Groves and Jiang 2013; Peyraud et al. 2013; Hsu et al. 2015; Hsu 2018; Ng and Hsu 2021). Recently, Ng and Hsu (2021) applied the 3D building model for RTK with detecting and excluding NLOS affected measurements, and the 3DMA RTK can provide a 10-cm-level positioning accuracy on average in a medium urban area, which demonstrates the benefit of the 3DMA method to classic GNSS precise positioning techniques.

Therefore, to improve the performance of urban PPP-RTK, this study focuses on realizing 3DMA PPP-RTK. Considering the common issue of insufficient satellites in urban canyons, a novel 3DMA weighting algorithm is developed instead of the rough excluding strategy. The reason behind is to avoid the distortion of the dilution of precision (DOP) after the exclusion of NLOS measurements (Zhang et al. 2018). In addition, the proposed weighting algorithm can be widely applied to existing advanced methods of GNSS precise positioning. In other words, it can be used in the noise covariance of the measurement vector by indicating the severity of multipath effects. We believe the proposed weighting algorithm will be useful and convenient for the researchers in the geodesy community. The remainder of this study is

organized as follows. We will introduce the methods of PPP-RTK and the proposed algorithm first. Then, the data and experiment settings are described. In the next part, the data analysis for building weighting functions and the results of 3DMA PPP-RTK static and kinematic experiments are given. Afterwards, extended discussions about urban PPP-RTK are carried out. Conclusions are drawn in the last section.

2 Methods

2.1 PPP-RTK server and client implementation

Generally, the PPP-RTK platform consists of two parts: the PPP-RTK server and client ends. The PPP-RTK in this study is built based on the undifferenced uncombined PPP model with applying not only the satellite orbit and clock products in the state space but also the satellite phase bias product and the atmospheric products in the state space (Wübbena et al. 2005). The PPP-RTK server end is generating all kinds of satellite-related and atmospheric corrections, especially for the ionospheric and tropospheric corrections. The client end can realize precise positioning based on the PPP model with the detailed SSR. The main difference between PPP and PPP-RTK is that PPP-RTK has more complete correction products and constraints. The main difference between RTK and PPP-RTK is that PPP-RTK eliminates the errors (e.g., clock errors and atmospheric errors) of the space state while RTK eliminates the errors by making differences of pseudorange and carrier-phase observations among different stations and different satellites. Namely, PPP-RTK is SSR-based while RTK is OSR-based.

The following Eq. (1) shows the raw GNSS measurement model in the case of multi-GNSS data,

$$\begin{cases} P_{i,1}^j = \rho_i^j + c\left(t_i^S - t^j\right) + m_i^j T_i + I_i^j + d_{i,1}^S - d_1^j \\ P_{i,2}^j = \rho_i^j + c\left(t_i^S - t^j\right) + m_i^j T_i + \mu_S^2 I_i^j + d_{i,2}^S - d_2^j \\ \lambda_{S,1}\varphi_{i,1}^j = \rho_i^j + c\left(t_i^S - t^j\right) + m_i^j T_i - I_i^j \\ +\lambda_{S,1}\left(N_{i,1}^j + b_{i,1}^S - b_1^j\right) \\ \lambda_{S,2}\varphi_{i,2}^j = \rho_i^j + c\left(t_i^S - t^j\right) + m_i^j T_i - \mu_S^2 I_i^j \\ +\lambda_{S,2}\left(N_{i,2}^j + b_{i,2}^S - b_2^j\right) \end{cases} \tag{1}$$

where $P_{i,1}^j$, $P_{i,2}^j$, $\varphi_{i,1}^j$, $\varphi_{i,2}^j$ are the pseudorange and carrier-phase observations from satellite j to receiver i for L1 and L2 frequencies (L1 and L2 for GPS satellites, E1 and E5a for Galileo satellites, B1I and B2I for BDS-2, B1C and B2a for BDS-3). ρ_i^j is the geometric distance between satellite j and receiver i. c is the velocity of light. t_i^S is the receiver clock for the satellite system S. Each system will have an individual receiver clock to handle the inter-system bias. m_i^j is the mapping function for mapping the zenith tropospheric delay T_i to the line-of-sight direction. I_i^j is the ionospheric delay on the L1 signal for satellite j. μ_S is the coefficient for the ionospheric delay which equates to $\frac{f_{S,1}}{f_{S,2}}$. $f_{S,1}$ and $f_{S,2}$ are the frequencies of L1 and L2 for satellite system S. $\lambda_{S,1}$ and $\lambda_{S,2}$ are the wavelength of L1 and L2 signals. $N_{i,1}^j$ and $N_{i,2}^j$ are integer ambiguities. $d_{i,1}^S$, $d_{i,2}^S$, d_1^j, d_2^j are hardware delays for pseudorange measurements at the satellite and the receiver ends, respectively. $b_{i,1}^S$, $b_{i,2}^S$, b_1^j, b_2^j are the hardware delays for carrier-phase measurements at the satellite and the receiver ends, respectively. To overcome the rank deficiency of adjustment caused by the linear dependency between hardware delays and clock parameters (Odijk et al. 2016), the re-parameterization will be realized in our PPP-RTK processing.

The PPP-RTK platform realized in this study is displayed in Fig. 1. The server end is responsible for providing the IGS satellite products including orbit, clock and code OSB (observable-specific signal bias), the phase OSB generation module and the atmospheric correction generation module (Geng et al. 2022).

To estimate the re-parameterized parameters that absorb related hardware biases, $\hat{t}_i^S$, $\hat{I}_i^j$ and $\hat{N}_{i,1}^j$, $\hat{N}_{i,2}^j$, and the parameter T_i at the server end, the measurement models after considering all modeled and known corrections, l_{i,P_1}^j, l_{i,P_2}^j, l_{i,L_1}^j, l_{i,L_2}^j (e.g. geometric distance, satellite clock, antenna phase center), are given as following:

$$\begin{cases} P_{i,1}^j - l_{i,P_1}^j = c\hat{t}_i^S + m_i^j T_i + \hat{I}_i^j \\ P_{i,2}^j - l_{i,P_2}^j = c\hat{t}_i^S + m_i^j T_i + \mu_S^2 \hat{I}_i^j \\ \lambda_{S,1}\varphi_{i,1}^j - l_{i,L_1}^j = c\hat{t}_i^S + m_i^j T_i - \hat{I}_i^j + \lambda_{S,1}\hat{N}_{i,1}^j \\ \lambda_{S,2}\varphi_{i,2}^j - l_{i,L_2}^j = c\hat{t}_i^S + m_i^j T_i - \mu_S^2 \hat{I}_i^j + \lambda_{S,2}\hat{N}_{i,2}^j \end{cases} \tag{2}$$

As for the PPP-RTK server, by fixing the known reference stations' coordinates, satellite precise clock and satellite precise orbit, the float ambiguities $\hat{N}_{i,1}^j$ and $\hat{N}_{i,2}^j$ could be estimated. The L1 and L2 float ambiguities collected from a global/regional GNSS station network are next used to calculate the phase OSBs (Schaer et al. 2021; Geng et al. 2022). Note that satellite clocks need to be re-estimated after identifying the phase biases (Geng et al. 2019).

The atmospheric correction generation module can compute the ambiguity-fixed satellite-station-specified ionospheric delays and the ambiguity-fixed station-specified tropospheric delays with the help of the known coordinates and the generated phase OSBs above. Thus, we can interpolate atmospheric corrections based on the station distribution. As Eq. (3) shows, IDW (inverse distance weighting) method

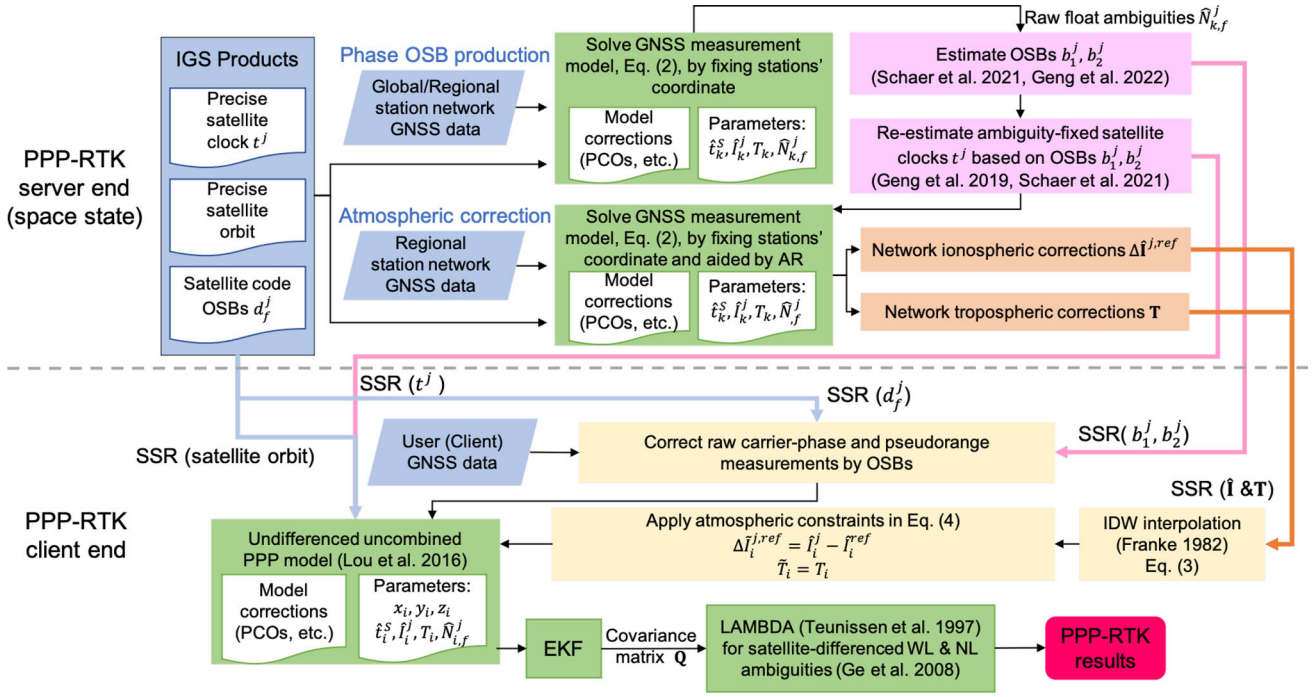

Fig. 1 Structure of the PPP-RTK platform in this study

(Franke 1982) is used in this study. k is the index of the reference station, and n is the number of reference stations. $\mathrm{dist}_{i,k}$ denotes the geometric distance between user i and the reference station k. γ is the exponential value for IDW, and the user can tune it based on the actual performance of the interpolation. γ is set as 1 in this paper.

$$\Delta\tilde{I}_i^{j,\mathrm{ref}} = \sum_{k=1}^{n}\left(\frac{\mathrm{dist}_{i,k}^{-\gamma}}{\Sigma_{k=1}^{n}\left(\mathrm{dist}_{i,k}^{-\gamma}\right)}\cdot\Delta\hat{I}_k^{j,\mathrm{ref}}\right) \tag{3}$$

Note that the raw ionospheric delay $\hat{I}_i^j$ of each station-satellite pair will absorb some receiver-specified hardware biases, so the operation of the single-difference between satellites should be carried out by selecting a reference satellite (with superscript ref) to eliminate the receiver-specified errors in the raw ionospheric delays and get the single-difference ionospheric delay $\Delta\hat{I}_k^{j,\mathrm{ref}}$. Only if the receiver-specified errors in raw ionospheric delays are eliminated, the subsequent interpolation of the network can be carried out correctly. Namely, the client end will interpolate satellite-pair ionospheric delay $\Delta\tilde{I}_i^{j,\mathrm{ref}}$ and the tropospheric delay $\tilde{T}$ for use.

The client end is based on the undifferenced uncombined PPP model, and the EKF (extended Kalman filter) is adopted to realize the parameter estimation. Compared with the classic PPP with ambiguity resolution, the PPP-RTK in this study can be achieved by adding tight atmospheric constraints to accelerate the convergences of relevant parameters so that ambiguities can be quickly resolved and the positions will be improved significantly. As Fig. 1 shows, based on the atmospheric corrections generated from the server end, they can be regarded as constraints in pseudo-observation and be added to the model, i.e., the last two rows in Eq. (4). The form can be

$$\begin{cases} P_{i,1}^j - l_{i,P_1}^j = -\boldsymbol{\alpha}_{i,1}^j\cdot\boldsymbol{x}_i + c\hat{t}_i^S + m_i^j T_i + \hat{I}_i^j \\ P_{i,2}^j - l_{i,P_2}^j = -\boldsymbol{\alpha}_{i,2}^j\cdot\boldsymbol{x}_i + c\hat{t}_i^S + m_i^j T_i + \mu_S^2\hat{I}_i^j \\ \lambda_{S,1}\varphi_{i,1}^j - l_{i,L_1}^j = -\boldsymbol{\alpha}_{i,1}^j\cdot\boldsymbol{x}_i + c\hat{t}_i^S + m_i^j T_i - \hat{I}_i^j + \lambda_{S,1}\hat{N}_{i,1}^j \\ \lambda_{S,2}\varphi_{i,2}^j - l_{i,L_2}^j = -\boldsymbol{\alpha}_{i,2}^j\cdot\boldsymbol{x}_i + c\hat{t}_i^S + m_i^j T_i - \mu_S^2\hat{I}_i^j + \lambda_{S,2}\hat{N}_{i,2}^j \\ \Delta\tilde{I}_i^{j,\mathrm{ref}} = \hat{I}_i^j - \hat{I}_i^{\mathrm{ref}} \\ \tilde{T}_i = T_i \end{cases} \tag{4}$$

where $\boldsymbol{\alpha}_{i,1}^j$, $\boldsymbol{\alpha}_{i,2}^j$ are the unit vectors from receiver i to satellite j. $\boldsymbol{x}_i$ denotes the correction position vector relative to the initial guess of the user coordinates. After the measurement update of the EKF, the raw ambiguities are mapped into satellite-pair wide-lane (WL) ambiguities. Then, the mapped covariance matrix is injected into the LAMBDA (the least-squares ambiguity decorrelation adjustment) method (Teunissen et al. 1997) to search for the integer WL ambiguities, and the parameters will be updated based on the new covariance matrix. After the WL ambiguities are fixed, the narrow-lane (NL) ambiguities can be deduced and the covariance matrix can also be mapped into a new matrix

with the satellite-pair NL ambiguities. In the same way, the new covariance matrix based on the NL ambiguity will be injected into the LAMBDA method for searching the integer NL ambiguities (Ge et al. 2008). We can obtain the final ambiguity-fixed result of PPP-RTK through the parameter update (Dong and Bock 1989). Note that partial ambiguity fixing is adopted for obtaining a better success rate.

2.2 3DMA, C/N_0 and elevation-angle-dependent weighting functions

In general, a weighting function can be modeled based on analyzing measurement errors. The key point is to find the relationship between the error and the selected parameter, and the selected parameter should have a significant correlation with the measurement error. By the ray-tracing algorithm, signals can be classified into LOS, NLOS and multipath (combination of reflection and line-of-sight signals). According to a general distribution of different receptions in a skyplot (Icking et al. 2020), LOS receptions are in an area higher than the building boundary. Reflection-caused multipath is near the building boundary. NLOS receptions with big delays are in the area lower than the building boundary. Therefore, the difference between the elevation angle of the satellite and the elevation angle of the corresponding building boundary ΔElev is finally selected as the key parameter of our proposed 3DMA weighting function. As Fig. 2 shows, the background figure is a 'sky mask' which is a skyplot with the building boundary (Ng et al. 2019). A LOS satellite with green color signed 'B' and a NLOS satellite with red color signed 'D' are plotted. The point 'O' denotes the receiver location. 'A' and 'C' denote the corresponding positions of the building boundary for the two satellites. Thus, $\Delta\text{Elev}_{\overrightarrow{AB}} = \text{Elev}^B - \text{Elev}^A$ and $\Delta\text{Elev}_{\overrightarrow{CD}} = \text{Elev}^D - \text{Elev}^C$. $\Delta\text{Elev}_{\overrightarrow{AB}}$ is bigger than 0° and $\Delta\text{Elev}_{\overrightarrow{CD}}$ is smaller than 0°.

The measurement error ΔMeasurement here we adopted is the absolute value of the L1 pseudorange residual since it can better reflect the severity of multipath effects (Hsu 2017). To make sure the pseudorange residual can better reflect the actual pseudorange error, we carried out the PPP-RTK mentioned in Sect. 2.1 to obtain the converged coordinates of the static experiments by excluding the predicted NLOS receptions by 3D building models (the elevation angle of the satellite is smaller than the elevation angle of the corresponding building boundary). With the known coordinates and SSR information from the PPP-RTK server end, the ambiguity-fixed receiver clock could be estimated. Then, all corrections and parameters in the GNSS measurement model, Eq. (2), are known. We can therefore compute the pseudorange residuals by eliminating relevant corrections and estimated parameters from the pseudorange measurements based on Eq. (2).

The 3DMA weighting function is developed by drawing lessons from classic elevation-dependent weighting in the form of the exponential function (Euler and Goad 1991) and C/N_0 weighting (Realini and Reguzzoni 2013). The function W_{3DMA} indicates the behavior of the measurement error as a function of ΔElev values. It also takes the form of a piecewise function that consists of three segments considering the measurement error distribution in Sect. 4.1. When the ΔElev of a satellite is larger than the threshold deg T°_{3DMA}, a standard benchmark weighting, 1, is given. It means that the initial variance of the measurement will not be changed. The parts of $0° < \Delta\text{Elev} < T^\circ_{\text{3DMA}}$ and $\Delta\text{Elev} \leq 0°$ are modeled by two kinds of exponential functions. The 0° indicates the building boundary. The piecewise function is shown in Eq. (5). T°_{3DMA} is empirically set to 30°. Besides, the parameters including a_{3DMA}, b_{3DMA}, A_{3DMA}, and F°_{3DMA} indicate the specific shape of the fitting function. Specifically, a_{3DMA}, b_{3DMA} decide the bending of the exponential curve. F°_{3DMA} decides the ΔElev which the function will set the weight directly by A_{3DMA}. These kinds of parameters are usually tuned directly in many studies based on experimental data (Ng et al. 2020a). A more accurate determination used in this study was realized based on nonlinear least squares by modeling an optimization problem to fit the measurement error (https://github.com/ceres-solver/ceres-solver). Note that a suitable setting based on experiences can also achieve similar performance relative to the accurate determination.

$$W_{\text{3DMA}}(\Delta\text{Elev}) = \begin{cases} 1, & \Delta\text{Elev} \geq T^\circ_{\text{3DMA}} \\ 10^{-\frac{\Delta\text{Elev}-T^\circ_{\text{3DMA}}}{b_{\text{3DMA}}}} & 0° < \Delta\text{Elev} < T^\circ_{\text{3DMA}} \\ 10^{-\frac{\Delta\text{Elev}-T^\circ_{\text{3DMA}}}{a_{\text{3DMA}}}} \left(\left(\frac{A_{\text{3DMA}}}{10^{-\frac{F^\circ_{\text{3DMA}}-T^\circ_{\text{3DMA}}}{a_{\text{3DMA}}}}} - 1 \right) \frac{\Delta\text{Elev}-T^\circ_{\text{3DMA}}}{F^\circ_{\text{3DMA}}-T^\circ_{\text{3DMA}}} + 1 \right), & \Delta\text{Elev} \leq 0° \end{cases} \tag{5}$$

The C/N_0 weighting proposed by Realini and Reguzzoni (2013) is also used in this study. In Eq. (6), CN denotes the value of C/N_0 and parameters (T_{C/N_0}, F_{C/N_0}, a_{C/N_0}, A_{C/N_0}.) are also set based on nonlinear least squares.

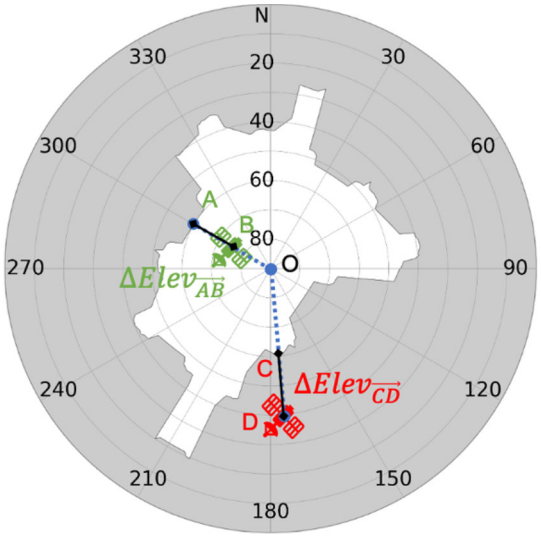

Fig. 2 Illustration of ΔElev in a sky mask. The elevation angle difference of each black line denotes the ΔElev of each satellite

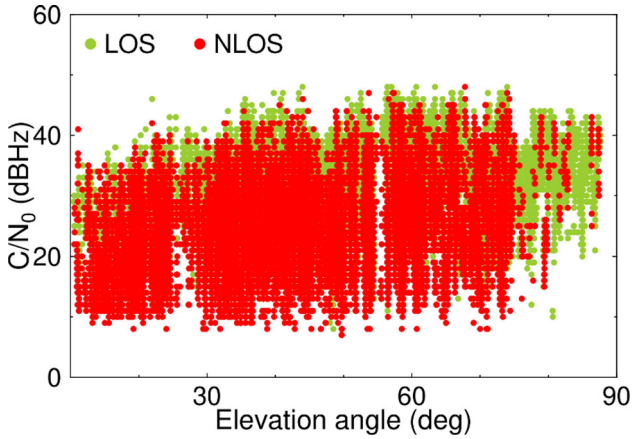

Fig. 3 LOS and NLOS distributions in C/N_0, and elevation angle of an open-source dataset in *Kaggle*. (https://www.kaggle.com/competitions/gnss-classification/data)

All weighting functions indicate the behavior of the measurement error as a function of corresponding parameters, e, C/N_0, and ΔElev. Importantly, 3DMA weighting aims to compensate for the insufficiency of other weighting methods (which is the multipath/NLOS effect with high-elevation angles and high-C/N_0) like elevation-angle-dependent weighting and C/N_0 weighting but not replace them. Figure 3 shows a distribution of LOS and NLOS of an open-source dataset. We can see many NLOS receptions (assuming $\Delta\text{Elev} < 0$) with high-C/N_0 and high-elevation angle.

Thus, we will combine them to generate the proposed final weighting. The combination strategy is shown in Eq. (8). Considering that C/N_0 weighting and 3DMA weighting are both concluded based on the same measurement errors, there is probably some shared information used. We use a linear function to combine them by fitting the measurement error ΔMeasurement. α and β are their coefficients, and we assume $\alpha + \beta = 1$. After obtaining the W_{C/N_0} and W_{3DMA} of all data (assuming there are n measurements) which indicate the behavior of the measurement error, the least square estimation in Eq. (9) to fit the measurement error can be carried out for estimating α and β. σ_0 is the unit of the measurement error and it can also be obtained when we do the fitting. For the classic elevation-angle-dependent weighting method, it is widely used for the data processing of GNSS base stations in open-sky environments, reflecting the common errors in the signal propagation (e.g. atmospheric error and multipath in the vertical direction). Thus, we generate the final error prediction by calculating the product of the $W_{\text{Elev}}(e)$ and the combination of $W_{C/N_0}(CN)$ and $W_{\text{3DMA}}(\Delta\text{Elev})$. Note that the outputs of all weighting functions above are used as the scale factor for the standard deviation of the measurement error in the position estimation of PPP-RTK while not used as weights of measurements directly.

$$W(\Delta\text{Elev}, CN, e) = W_{\text{Elev}}(e) \cdot \left(\alpha W_{C/N_0}(CN) + \beta W_{\text{3DMA}}(\Delta\text{Elev})\right) \tag{8}$$

$$W_{C/N_0}(CN) = \begin{cases} 1, & CN \geq T_{C/N_0} \\ 10^{-\frac{CN - T_{C/N_0}}{a_{C/N_0}}} \left(\left(\frac{A_{C/N_0}}{10^{-\frac{F_{C/N_0} - T_{C/N_0}}{a_{C/N_0}}}} - 1 \right) \frac{CN - T_{C/N_0}}{F_{C/N_0} - T_{C/N_0}} + 1 \right), & CN < T_{C/N_0} \end{cases} \tag{6}$$

Equation (7) shows the classic elevation-angle-dependent strategy which is also used in this study. e denotes the elevation angle.

$$W_{\text{Elev}}(e) = \begin{cases} 1, & e \geq 30^\circ \\ \frac{1}{2\sin(e)}, & e < 30^\circ \end{cases} \tag{7}$$

$$\begin{cases} \sigma_0 \begin{bmatrix} W_{C/N_0,1} & W_{\text{3DMA},1} \\ \vdots & \vdots \\ W_{C/N_0,n} & W_{C/N_0,n} \end{bmatrix} \cdot \begin{bmatrix} \alpha \\ \beta \end{bmatrix} = \begin{bmatrix} \Delta\text{Measurement}_1 \\ \vdots \\ \Delta\text{Measurement}_n \end{bmatrix} \\ \alpha + \beta = 1 \end{cases} \tag{9}$$

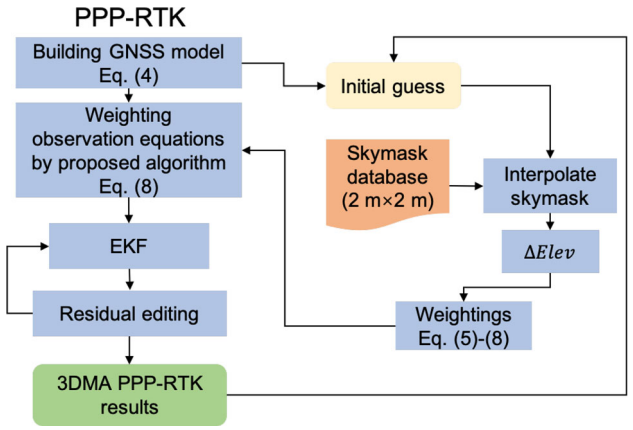

Fig. 4 The flowchart of 3DMA PPP-RTK

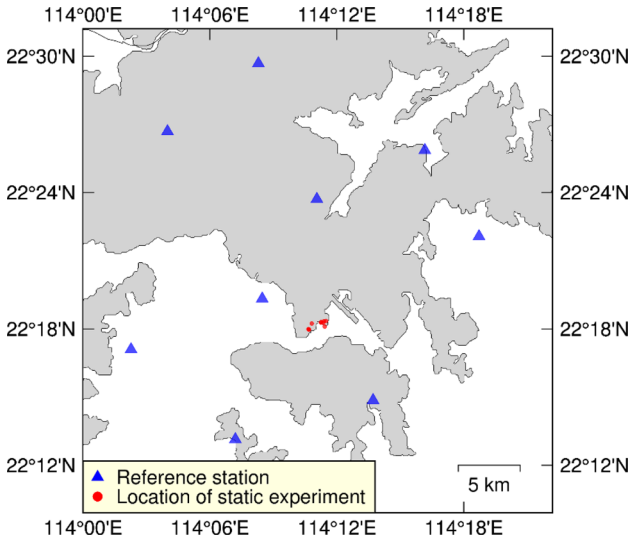

Fig. 5 Distribution of reference stations used for the developed PPP-RTK server

2.3 3DMA PPP-RTK

The flowchart of 3DMA PPP-RTK is displayed in Fig. 4. The left part shows the processing flow of the PPP-RTK client end and the right part is the processing of 3D building model processing. As for 3DMA PPP-RTK, the proposed 3DMA weighting should be achieved before the measurement update of EKF. The processing of the 3D building model aims to compute the ΔElev. To reduce the real-time computational load, a pre-generated database of sky mask was built (Ng et al. 2020b). The database collects sky masks of candidates in all non-building areas in the form of a 2 × 2-m grid based on the latitude and longitude. The sky masks of users can therefore be interpolated according to the initial guess of the position. The initial guess can be obtained by single point positioning with pseudoranges or the PPP-RTK result of the previous epoch. It is noted that a poor initial guess of the position will probably deteriorate the performance of 3DMA weighting. Therefore, sometimes we need to update the initial guess by carrying out the EKF iteratively until acquiring a converged initial guess. After obtaining the ΔElev, all weightings could be achieved. After the parameter estimation, empirical residual editing for pseudorange, and carrier-phase observations will be carried out for discarding outliers. The thresholds for pseudorange and carrier-phase observations are 3 m and 0.03 m, respectively. Finally, the 3DMA PPP-RTK results will be output.

3 Data and experiments

To realize the PPP-RTK server processing, we selected 9 GNSS reference stations from the Hong Kong satellite positioning reference station network. As Fig. 5 shows, the reference stations cover the urban area of positioning experiments. The closest distance between the reference stations is about 10 km. In total, we collected 11 groups of static GNSS data in different levels (slight, medium, deep) of urban environments and one group of vehicle-borne kinematic data in a general medium urban environment. In both static and vehicle-borne experiments, the kinematic mode EKF-based user positioning is used for the user coordinates estimation. Also, the ambiguity resolution was in the continuous mode, which indicates the resolution was carried out in every epoch without a prior constraint of already fixed ambiguities. The ground truths of the trajectory of the vehicle-borne kinematic experiment were provided by the high-precision RTK/INS processing (SPAN combined system and IE software of NovAtel). The ground truths of the locations of all static experiments were provided by the converged results of 3DMA PPP-RTK. Table 1 gives the detailed data processing strategies of 3DMA PPP-RTK. Note that although BDS-3 observations could be obtained by the user, they were not used for the ambiguity resolution because the PPP-RTK server end lacks BDS-3 observations. In addition, BDS GEO satellites were excluded in our processing, considering their relatively poor accuracy.

The locations and the sky masks of the 11 static GNSS experiments are shown in Fig. 6. From (a) to (k), each subfigure shows the condition of each static experiment. We define the urbanization rate of a specific location by the mean sky mask elevation angle μ_m and the sky mask elevation angle standard deviation σ_m (Wen et al. 2020). N is the number of azimuth angles from the sky mask. The default spacing is 1°, so N is equal to 360. e_a denotes the boundary elevation at the azimuth angle a. Table 2 shows the μ_m and σ_m values of all static experiments. In general, if the location is in a deep urban canyon, the high-rise structures will result in a large μ_m and a relatively small σ_m. When μ_m is large, a larger σ_m will further deteriorate the satellite geometry.

Table 1 Detailed data processing strategies of the proposed 3DMA PPP-RTK

Items	Descriptions
Regional network for server	9 GNSS reference stations from Hong Kong satellite positioning reference station network (https://www.geodetic.gov.hk/en/satref/satref.htm) (GPS, Galileo, BDS-2)
Experiment data	11 groups of static GNSS data 1 group of kinematic GNSS data (GPS, Galileo, BDS-2, BDS-3)
GNSS measurements	Dual-frequency pseudorange and carrier-phase measurements from a NovAtel geodetic receiver (PwrPak7D) with an antenna (HXCGPS1000)
3D building model	Hong Kong 3D city model (https://www.landsd.gov.hk/en/spatial-data/open-data.html)
Sampling-rate	1 s of data for the PPP-RTK client end 30 s of data for the PPP-RTK server end
Elevation cut-off angle	10°
OSBs	Code OSBs from CAS (Chinese Academy of Sciences) (http://ftp.gipp.org.cn) Phase OSBs generated from PPP-RTK server end
Antenna phase center	*igs14.atx* for satellite antenna PCOs and PCVs
Tide displacements	Solid earth tides, pole tides and ocean tidal loading (Petit and Luzum 2010; Lyard et al. 2006)
Troposphere delays	Saastamoinen model supplied the priori values, and GMF mapping function was adopted (Saastamoinen 1972; Boehm et al. 2006)
Slant ionospheric delays	Estimated as random-walk parameters
Satellite orbits and clocks	Using the rapid precise satellite orbit and precise satellite clock products of GFZ (ftp://ftp.gfz-potsdam.de)
Receiver clocks	Estimated as white noise like parameters
Ambiguities	Estimated as constants over each continuous arc
Tropospheric constraint	Constraints of centimeter-level (2 cm) noises in Eq. (4)
Ionospheric constraint	Constraints of centimeter-level (5 cm) noises in Eq. (4)
Station coordinates	For server: fixing the known coordinates For client: estimated as random-walk parameters

$$\mu_{\mathrm{m}} = \frac{\sum_{a=1}^{N} e_a}{N} \tag{10}$$

$$\sigma_{\mathrm{m}} = \sqrt{\frac{\sum_{a=1}^{N} (e_a - \mu_{\mathrm{m}})^2}{N-1}} \tag{11}$$

According to the specific conditions of all static experiments in Hong Kong, the 11 locations are classified into three kinds of urban environments (slight, medium, and deep). The slight urban environment has a μ_{m} less than 30°. The medium urban environment has a μ_{m} larger than 30° but less than 50°. The deep urban environment not only has a μ_{m} larger than 50°, but also has a σ_{m} larger than 10°. The subfigure (a) denotes one slight urban environment with small μ_{m} and σ_{m}. The subfigures (b) to (g) denote six medium urban environments. Note that although location (f) has a large μ_{m} equal to 45.11°, its σ_{m} is only 5.91° which means the geometry is still not bad. The subfigures (h) to (k) denote four deep urban environments. The red dot in each subfigure denotes the location. The sky mask is also plotted at the bottom left of each subfigure.

Figure 7 shows the trajectory of the vehicle-borne kinematic experiment. This trajectory is in a medium urban area basically. The start location of this trajectory is an intersection and the end location is the tunnel entrance. There are several complex environments during the trajectory which will cause a poor satellite geometry and few satellites, especially near the obstacles (i.e., buildings) plotted in the figure.

To analyze the performance of 3DMA PPP-RTK, we processed all experiments by four solutions, which are listed in Table 3. As for the urban precise positioning, we usually hope to achieve a decimeter-level accuracy that can target the applications such as lane-keeping for intelligent vehicles. Thus, in this study, if the horizontal positioning error is less than 20 cm, we regard these results are available and they have converged successfully.

4 Results

4.1 Demonstration of the 3DMA weighting and weighting combination

In this section, we will first ensure the effectivity of the selected parameter used in 3DMA weighting by correlation analysis. Then, tunning and fitting are tried to set suitable

Fig. 6 Locations of all the static experiments

Table 2 Mean values and standard deviations of sky mask elevation angles of all static experiments

Experiments	$\mu_m(^\circ)$	$\sigma_m(^\circ)$
(a)	17.73	14.14
(b)	37.70	13.11
(c)	36.85	15.02
(d)	42.22	16.40
(e)	40.17	15.91
(f)	45.11	5.91
(g)	37.76	13.00
(h)	55.33	13.50
(i)	55.95	11.90
(j)	51.88	13.38
(k)	55.58	13.76

parameters for relevant functions. Finally, we can obtain the results of the proposed combined weighting.

Considering there are a lot of multipath and NLOS receptions in the measurement errors, we used Spearman's rank correlation coefficient for analysis (Myers and Sirois 2006). The coefficient is not limited by the overall distribution shape and the sample size of the two variables. The measurement errors computed based on nine static GNSS data ((a)–(f) and (i)–(k)) are used for analysis. The static experiments (g) and (h) are regarded as the control group, and they are only used for the positioning experiments in the next section, but not for the weighting analysis. Note a few errors bigger than 10 m are excluded in the analysis based on our experiences. They are probably from serious NLOS receptions with huge delays (> 50 m), and the huge errors may contaminate the fitting. Figure 8 shows the results of the correlation analysis. The value in each grid ranged from -1 to 1 denotes the correlation coefficient between the corresponding ordinate object and the corresponding abscissa object. If the value is smaller than 0, the correlation is negative and the color is blue. On the contrary, the correlation is positive and the color is red. The bigger the absolute value is, the higher the correlation is.

Fig. 7 Reference trajectory of the vehicle-borne kinematic experiment

The left analysis uses all data and the right analysis uses the data with the measurement error bigger than 2 m. According to the results, we can see the correlation between the measurement error and C/N_0 and the correlation between the measurement error and ΔElev are both negative and significant. C/N_0 is significant considering all data. However, if we focus on big measurement errors, ΔElev with a coefficient of -0.37 is more significant than C/N_0 with a coefficient of -0.12. We think it is due to many measurements with NLOS and multipath receptions still having strong signal strengths. Therefore, the parameter ΔElev could be useful and it can augment the C/N_0 weighting.

According to the proposed weighting functions in Sect. 2.2, there are still several unknown parameters to be set. Thus, Fig. 9 shows the measurement errors with respect to C/N_0 and ΔElev values. The mean values are plotted to give a general view. By nonlinear least squares, the C/N_0 weighting adopts the parameters of $\left(T_{C/N_0} = 50,\ F_{C/N_0} = 25,\ a_{C/N_0} = 34,\ A_{C/N_0} = 43\right)$ when processing static data with the NovAtel geodetic receiver. The 3DMA weighting adopts the parameters of $\left(T^{\circ}_{\mathrm{3DMA}} = 30°,\ a_{\mathrm{3DMA}} = 35,\ b_{\mathrm{3DMA}} = 160,\ A_{\mathrm{3DMA}} = 32,\ F^{\circ}_{\mathrm{3DMA}} = -24°\right)$. We can see the predicted curves are close to the mean values. Interestingly, for the 3DMA weighting, we can see that ΔElev of 0° signifies whether the signal may be reflected and diffracted. This phenomenon is also the main reason why we divide the function into three segments. Figure 10 clearly shows the combined weighting surface $\left(0.615W_{C/N_0}(CN) + 0.385W_{\mathrm{3DMA}}(\Delta\mathrm{Elev})\right)$ of the measurement errors with respect to ΔElev and C/N_0. The estimation coefficients are obtained by Eq. (9). We can see that this fitting surface is closer to the actual distribution of the measurement errors. The two techniques are thus complementary. Although the parameters and coefficients in this study were accurately estimated based on parts of collected data, we think that they can be tried in other datasets with similar environments and GNSS receivers and antennas. Users can try to tune them based on experiences.

4.2 Positioning results of static experiments

In this section, the results of all static experiments will be shown and analyzed. The following three figures show three selected cases, and more results will be listed in Table 4. Figure 11 shows the results of the static experiment (g) in the medium urban environment, and we do not use the data of this experiment for the previous weighting analysis. We can find the result of the solution PPP-RTK_E-W is good with the RMSs of 1.3, 2.0 and 6.5 cm in three components. There are only a few wrong jump points, and the result still has a slight convergence process at the beginning. For the result of the solution PPP-RTK_E-C/N_0-W, we can find the positioning precision is improved, and the RMSs are 0.9, 1.1 and 5.1 cm. Successful ambiguity fixing is achieved instantaneously. But we can find the new processing still causes a few abnormal fluctuations in the up component. When using the 3DMA weighting, the positioning precision becomes better, with the RMSs of 0.9, 1.0 and 4.8 cm. In general, the results indicate that the classic PPP-RTK with elevation-angle-dependent weighting and residual editing can already obtain a good performance in a medium urban environment. Although C/N_0 weighting and 3DMA methods do not bring significant improvement, they still work on enhancing the results. In a slight and medium urban environment, although there will be NLOS and complex multipath receptions, good LOS signals still dominate the GNSS processing. The outliers could also be removed easily by common residual editing. However, we can find

Table 3 Solutions of PPP-RTK

Solutions	Descriptions
PPP-RTK_E-W	PPP-RTK with elevation weighting Equation (7)
PPP-RTK_E-C/N_0-W	PPP-RTK with elevation and C/N_0 weighting Equations (6) and (7)
PPP-RTK_E-3DMA-W	PPP-RTK with elevation and 3DMA weighting Equations (5) and (7)
PPP-RTK_E-C/N_0-3DMA-W	PPP-RTK with elevation, C/N_0 and 3DMA weighting Equations (5–8)

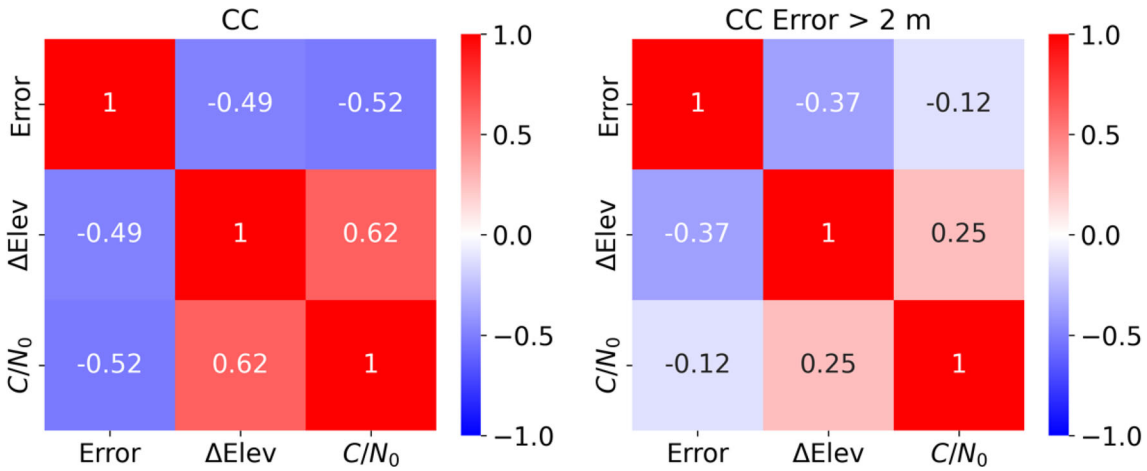

Fig. 8 CC (Correlation coefficient) analysis. The measurement error, C/N_0 and ΔElev are analyzed together. Different values and colors denote the correlation coefficients

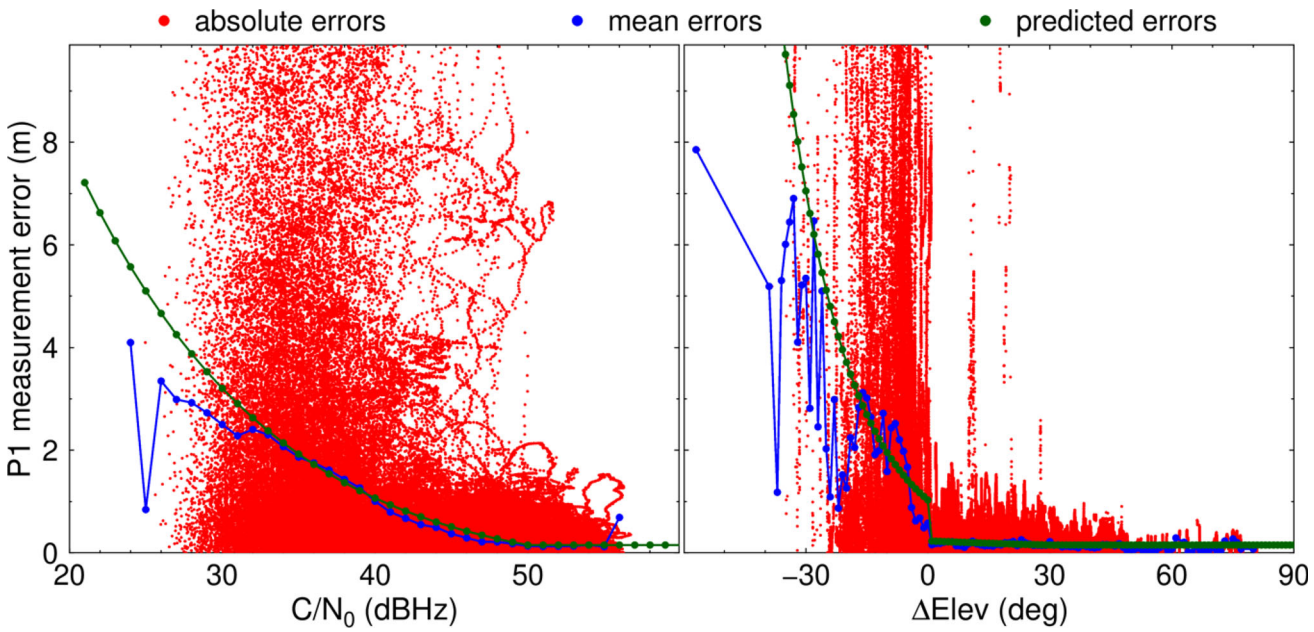

Fig. 9 Measurement errors with respect to C/N_0 values and with respect to ΔElev values. The blue lines denote the mean values and the green lines denote the predicted errors generated by corresponding weighting functions. The absolute errors are denoted by the red dot

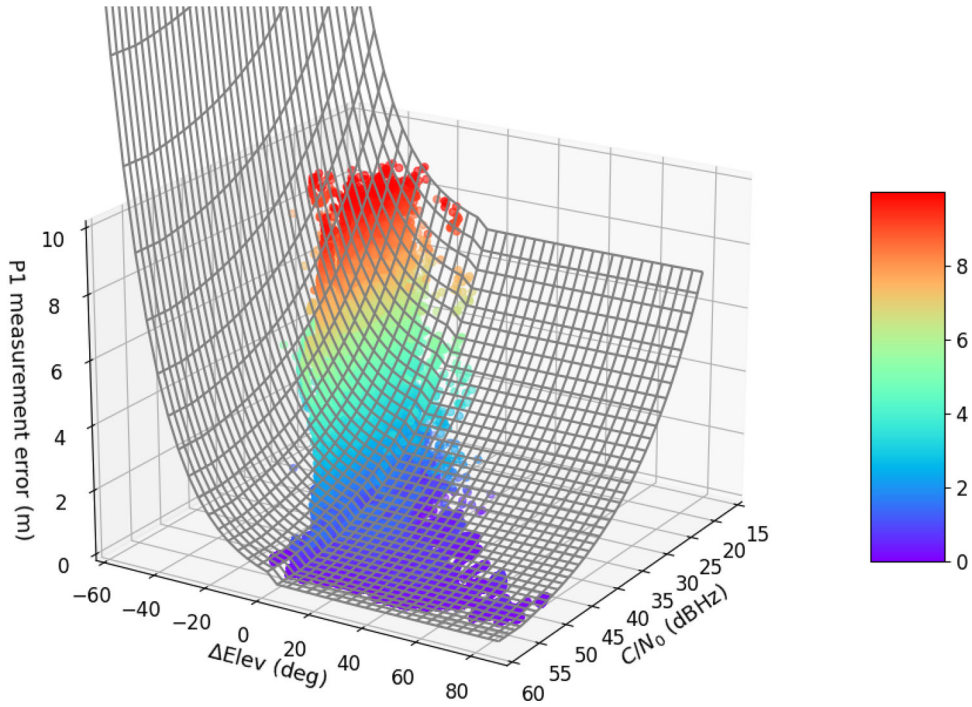

Fig. 10 Proposed weighting surface of combining ΔElev and C/N_0 weighting functions

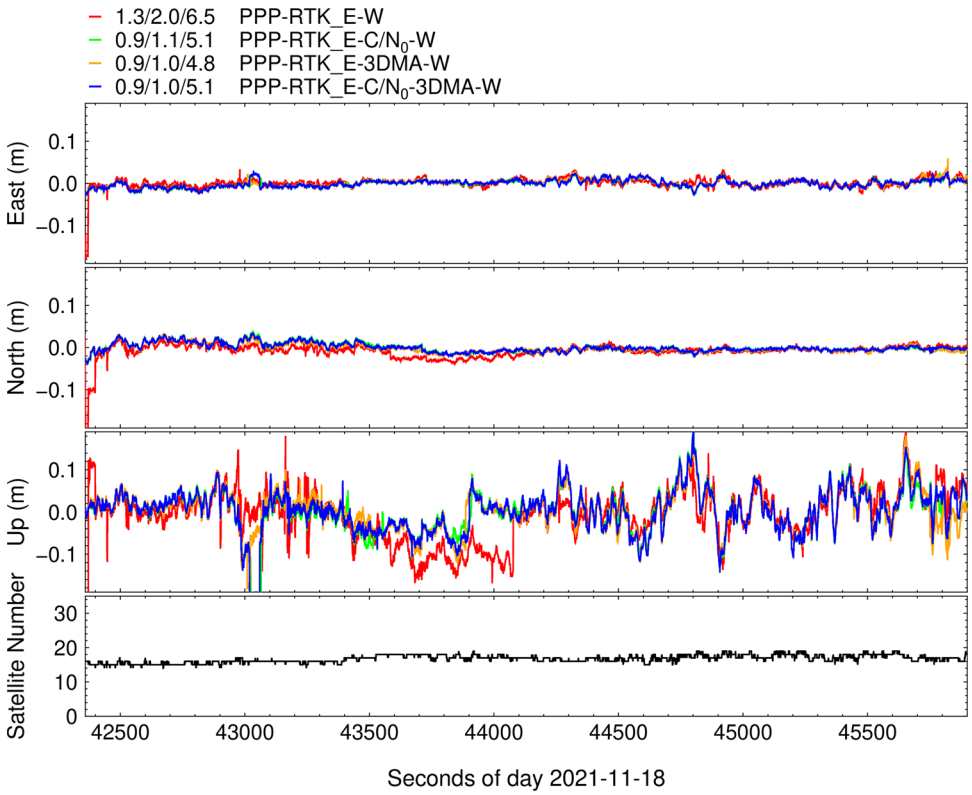

Fig. 11 Positioning errors in three components and the satellite numbers of the static experiment (g). The RMS values (cm) of the positioning errors in three components are also shown

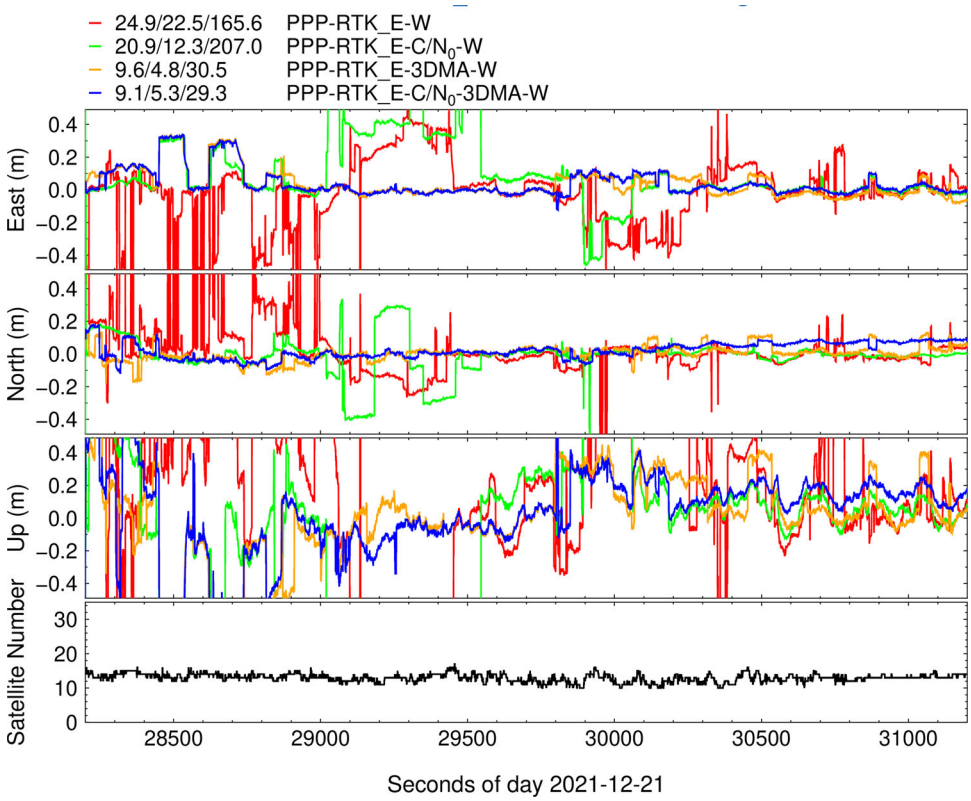

Fig. 12 Positioning errors in three components and the satellite numbers of the static experiment (h). The RMS values (cm) of the positioning errors in three components are also shown

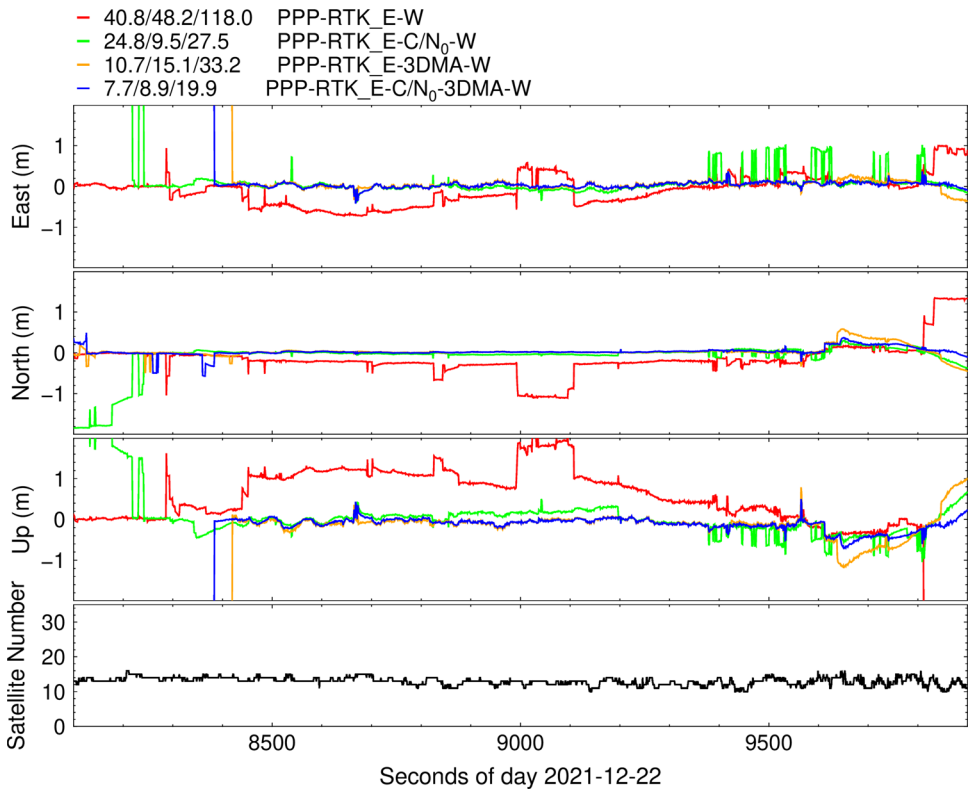

Fig. 13 Positioning errors in three components and the satellite numbers of the static experiment (k). The RMS values (cm) of the positioning errors (after 8500 s) in three components are also shown

the result of PPP-RTK_E-C/N_0-3DMA-W around 43,000 s is even worse than the result of PPP-RTK_E-W. The reason is probably that some observations with low C/N_0 and small ΔElev still retain good accuracy. The empirical C/N_0 and 3DMA weightings cannot deal with some abnormal conditions. Fortunately, the conditions are only a small number.

In slight-medium urban environments, the effects of 3DMA weighting and C/N_0 weighting do not seem very significant. However, for the results of static experiments in deep urban environments, the proposed 3DMA weighting algorithm could bring more significant improvements. Figures 12 and 13 show the results of the static experiments (h) and (k), respectively. According to Fig. 12 we can find the C/N_0 weighting does not significantly improve the horizontal positioning precision and it still has some abnormal fluctuations. However, introducing 3DMA weighting can improve the result dramatically. The RMSs of the results of PPP-RTK_E-C/N_0-3DMA-W are 9.1, 5.3 and 29.3 cm. We think this is because building-related errors are more dominant in this environment. The result of PPP-RTK_E-W is affected by poor observations, and the quality control means cannot deal with such complicated conditions (frequent multipath and NLOS receptions). The C/N_0 weighting still cannot distinguish all bad observations in the deep urban environment. So, the result of PPP-RTK_E-C/N_0-W still has a large fluctuation.

The location of the experiment (k) in Fig. 13 has a very complex environment among all locations. Although the mean available satellite number is about 11, there are about half satellites with $\Delta\text{Elev} < 0°$. According to the results, the horizontal positioning precision of PPP-RTK_E-W is sub-meter level. Only 33.3% of the epochs achieve available positioning precision. However, after applying the C/N_0 weighting, the horizontal positioning precision can be improved by more than 50%, and 77.2% of the results are available. C/N_0 weighting causes obvious convergence progress. Further using the 3DMA weighting, the horizontal precision after convergence can reach 15 cm and some poor results are improved. Although the positioning results after the convergence become more precise and stable, the added 3DMA weighting causes more obvious convergence progress (about 5 min) at the beginning which is not good for the positioning in a short time (several epochs). About 73.8% of the results are available. The phenomenon is likely due to some measurements are not suitably weighted. More analyses about the phenomenon are in the discussion section. Fortunately, the phenomenon is a special case in our experiments and the overall effectiveness of 3DMA weighting is still inspiring.

The results of all static experiments are listed in Table 4. The RMS results, the percentages of the epochs with successful convergence and the ambiguity-fixed rates are shown.

Table 4 Statistics for the results of all static experiments

ID	Urban canyon	Used in deducing weighting function?	PPP-RTK_E-W	PPP-RTK_E-C/N_0-W	PPP-RTK_E-3DMA-W	PPP-RTK_E-C/N_0-3DMA-W
(a)	Slight	Yes	1.9/2.9/8.2 (100%, 100%)	2.1/2.3/6.6 (100%, 100%)	1.6/2.1/7.0 (100%, 100%)	1.9/2.2/6.8 (100%, 100%)
(b)	Medium	Yes	1.0/1.6/6.8 (100%, 100%)	0.8/0.8/3.7 (100%, 100%)	0.8/0.8/3.7 (100%, 100%)	0.7/0.8/3.7 (100%, 100%)
(c)	Medium	Yes	6.6/4.6/5.4 (100%, 85.9%)	4.3/3.2/3.8 (100%, 97.2%)	6.0/4.2/4.0 (100%, 97.8%)	4.3/3.2/3.9 (100%, 97.7%)
(d)	Medium	Yes	2.8/4.0/8.3 (100%, 98.7%)	2.6/3.3/7.5 (100%, 100%)	1.0/1.1/7.4 (100%, 100%)	0.8/1.0/7.1 (100%, 100%)
(e)	Medium	Yes	3.5/3.4/9.5 (100%, 95.2%)	2.5/1.3/5.2 (100%, 100%)	4.1/2.0/8.0 (100%, 100%)	3.7/1.5/5.3 (100%, 100%)
(f)	Medium	Yes	3.1/1.0/10.2 (100%, 79.2%)	2.0/1.2/4.8 (100%, 100%)	2.5/1.5/4.9 (100%, 99.8%)	2.0/1.0/4.0 (100%, 100%)
(g)	Medium	No	1.3/2.0/6.5 (99.7%, 100%)	0.9/1.1/5.1 (100%, 100%)	0.9/1.0/4.8 (100%, 100%)	0.9/1.0/5.1 (100%, 100%)
(h)	Deep	No	24.9/22.5/165.6 (69.8%, 48.3%)	20.9/12.3/207.0 (75.6%, 63.7%)	9.6/4.8/30.5 (92.2%, 69.4%)	9.1/5.3/29.3 (93.5%, 78.1%)
(i)	Deep	Yes	8.3/3.9/65.3 (98.1%, 73.0%)	5.2/2.3/34.3 (100%, 84.5%)	6.5/2.7/25.1 (100%, 85.6%)	5.7/3.0/26.8 (100%, 86.6%)
(j)	Deep	Yes	66.6/111.9/231.8 (35.3%, 54.9%)	14.2/9.9/20.3 (92.2%, 97.0%)	7.7/4.8/13.5 (95.2%, 99.2%)	8.0/5.3/16.8 (99.0%, 98.3%)
(k)	Deep	Yes	40.8/48.2/118.0 (33.3%, 32.9%)	24.8/9.5/27.5 (77.2%, 59.9%)	10.7/15.1/33.2 (68.9%, 54.7%)	7.7/8.9/19.9 (73.8%, 57.6%)

The RMS values (cm) in three components (East, North and Up) and the percentages of the available results (left) and the ambiguity-fixed rates (right) are listed

We used the ratio test to decide if the candidate integer solution would be selected. The threshold of 3.0 was used in all experiments. According to the results, we can find that in the slight and medium urban environments, the effects of the proposed weighting are limited but it can still improve results slightly. In deep urban environments, it is hard for PPP-RTK to realize centimeter-level positioning. By applying the proposed weighting, the precision and the availability are both improved a lot. The 3DMA PPP-RTK could obtain more than 90% results with < 20 cm horizontal positioning precision. The ambiguity-fixed rates decrease obviously in deep urban environments relative to in slight-medium environments. After applying C/N_0 and 3DMA weightings, successful ambiguity resolution could be achieved at more epochs. For most experiments in deep urban environments, 3DMA weighting can further increase the fixed rates relative to the results with only C/N_0 weighting. In addition, we can find C/N_0 weighting and 3DMA weighting are not always effective in every experiment while combining them can obtain more stable and reliable results. The C/N_0 weighting cannot better evaluate some poor measurements with high-C/N_0. The 3DMA weighting will also be devalued by the building model with poor accuracy and non-building obstacles (e.g., trees). We think the 3DMA weighting can be complementary to the classic C/N_0 weighting.

4.3 Positioning results using vehicle-borne data

Besides the static experiments, the processing of one vehicle-borne kinematic experiment was also carried out. In general, the urbanization level along the trajectory is medium-level. Note that no matter the C/N_0 values or the multipath and NLOS receptions, the characteristics in the kinematic experiment are different from those in the static experiments. In the kinematic experiments, the C/N_0 values will become smaller and the multipath is changing quickly. We adjusted the parameters of the weighting function. The parameters $\left(T_{C/N_0} = 40,\ F_{C/N_0} = 20,\ a_{C/N_0} = 30,\ A_{C/N_0} = 30\right)$ of C/N_0 weighting are used based on our experience (Ng et al 2020a). The parameters of 3DMA weighting are assumed not changed. According to the results, we can find there are several big fluctuations. The C/N_0 weighting can improve a lot but it remains some abnormal results. By introducing the 3DMA weighting, the results are further improved. More than 90% of the results are available while the raw PPP-RTK only outputs about 55.2% of available results. The ambiguity-fixed rate also rises from 75.5% to more than 86% with the help of the weightings. The results further indicate the effectiveness of using the 3DMA weighting for urban PPP-RTK (Fig. 14).

5 Discussions

5.1 Convergence issue caused by improper measurement weighting

For the results of the experiment (k) in Sect. 4.2, the 3DMA weighing causes an obvious convergence process. Although the solution PPP-RTK_E-W obtains unsatisfied results throughout the period, it obtains better results at the beginning relative to other solutions. We think some measurements were not weighted accurately. As we know, DOP is to state how the measurement error will affect the final state estimation, indicating a mathematical effect of satellite geometry on positioning precision (Langley 1999). However, we cannot assume all measurements are independent with the same precision level in practice. The weighted DOP has been proved more accurate than the conventional DOP on representing the position error trends (Won et al. 2012). In other words, although all satellites were not excluded in our processing and it seems that we maintain the dilution of precision, the unsuitable weightings worsen it. We suggest the use of weighting should consider its effects on the weighted DOP, although it is difficult for us to evaluate measurements precisely. Furthermore, we tried to only apply the weighting to some selected satellites with large predicted measurement errors tentatively, and the new solution is named PPP-RTK_E-C/N_0-3DMA-W_D. According to the results in Fig. 15, the convergence progress is almost avoided and up to 96.7% of results are available. The results confirm there are some measurements need not be weighted. However, the way of selecting only works in post-processing. Better use of weighting and selection of measurements still need further research.

5.2 Instantaneous solution

The positioning results in Sect. 4 are all based on EKF and the filtering can obtain a good positioning result after convergence. We here consider the condition of instantaneous (one-epoch) positioning for some time-critical applications. Figure 16 shows the instantaneous positioning results of the static experiment (g). Surprisingly, for PPP-RTK_E-W, there are a lot of epochs with failed ambiguity resolution, and only 65.4% of the results are available. Once applying the proposed weighting algorithm, the positioning results are significantly improved. About 99.5% of the results are available. In urban environments with frequent multipath and NLOS receptions, it is difficult for classic PPP-RTK to achieve instantaneous centimeter-level positioning stably. The results indicate the importance of the weightings when processing the GNSS data in complex urban environments.

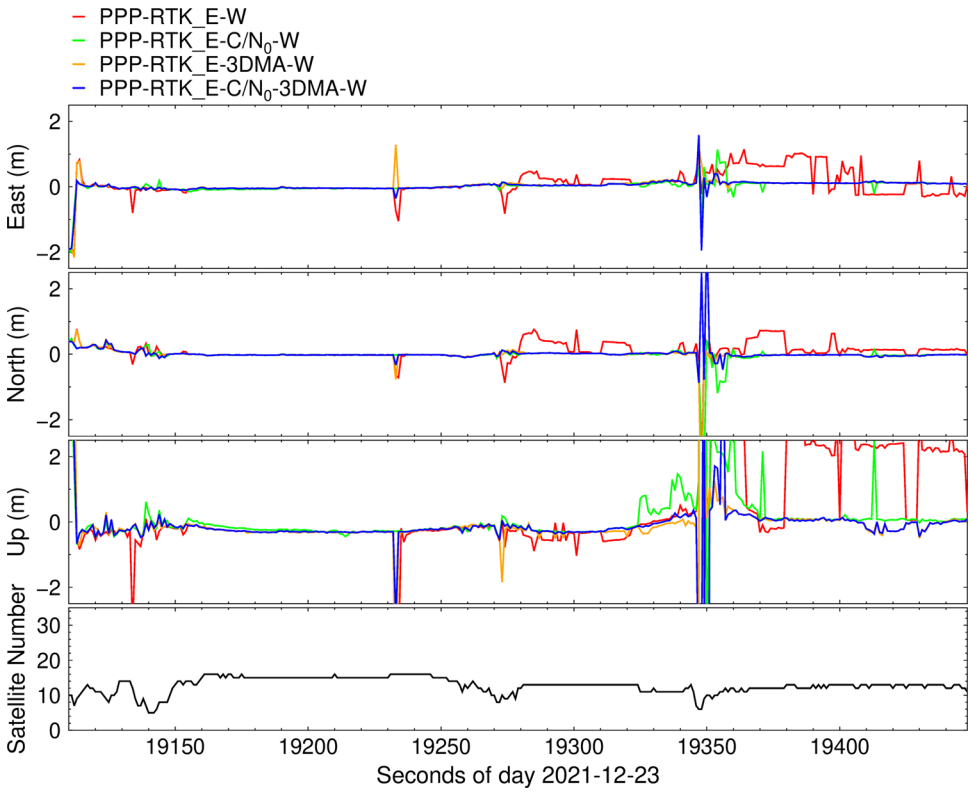

Fig. 14 Positioning errors in three components and the satellite numbers of vehicle-borne experiment

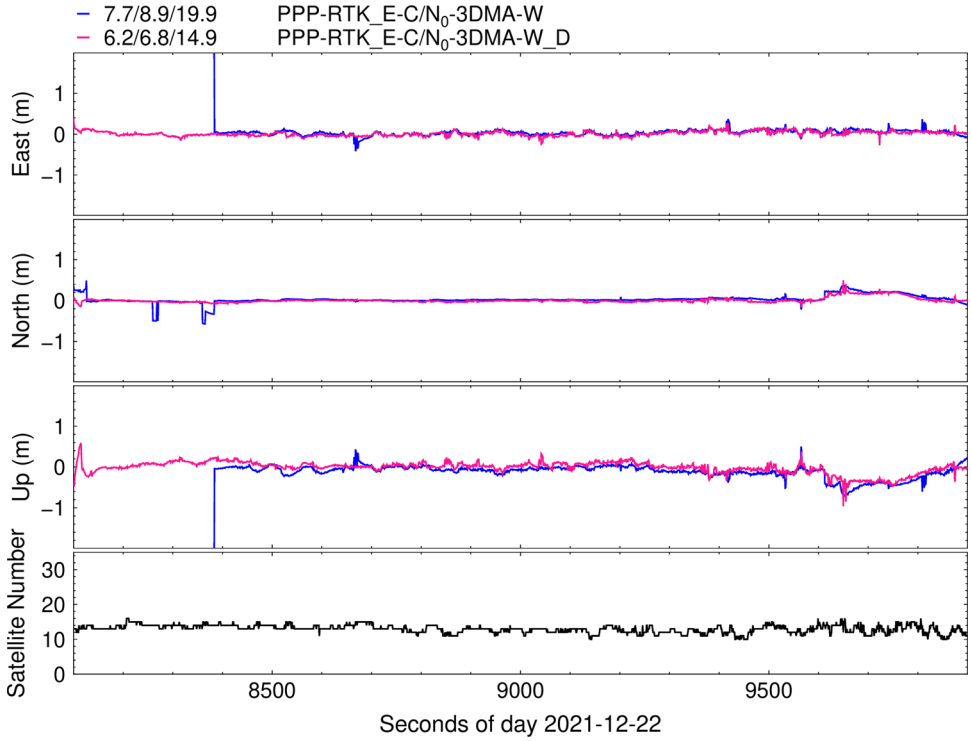

Fig. 15 Positioning errors in three components and the satellite numbers of static experiment (k). The RMS values (cm) of the positioning errors (after 8500 s) in three components are also shown

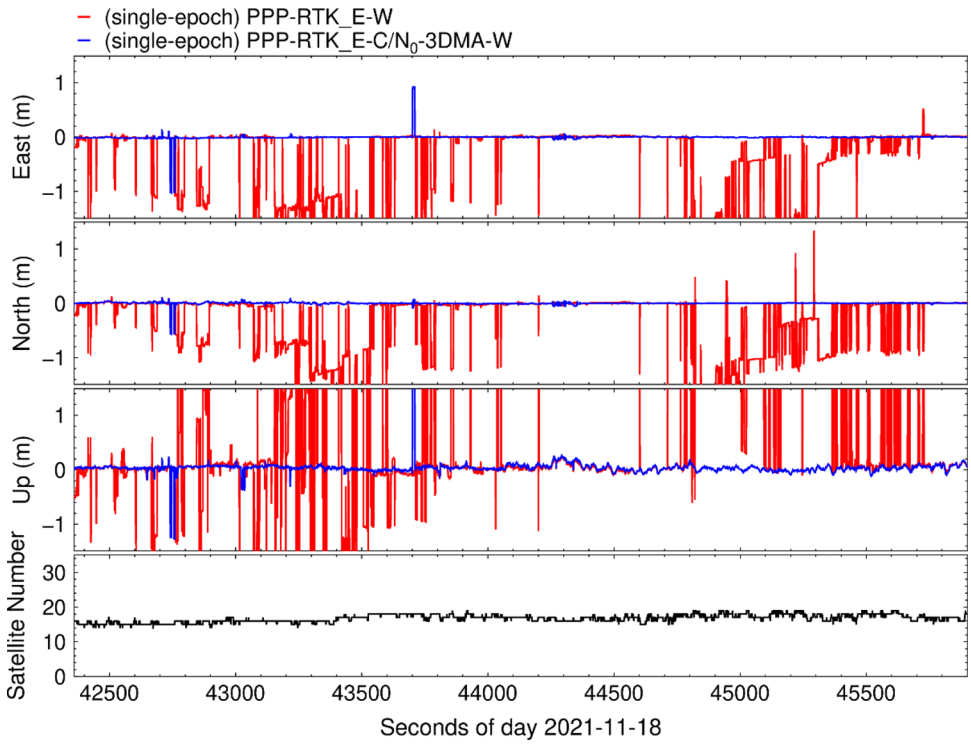

Fig. 16 Instantaneous positioning errors in three components

6 Conclusions and outlook

To enhance the performance of PPP-RTK in complex urban scenarios and inhibit the deterioration caused by frequent multipath and NLOS receptions, a novel 3D-mapping-aided weighting algorithm is provided in this study. We developed a PPP-RTK platform based on the undifferenced uncombined PPP-RTK model first. The server end generates the phase OSBs and atmospheric corrections. The client end introduces the atmospheric corrections by regarding them as constraints in a form of measurement. The difference between the satellite elevation angle and the elevation angle of the corresponding building boundary ΔElev is adopted for the 3DMA weighting function. We investigated the proposed weighting function by analyzing the correlation and the fitting performance. The results indicate that the 3DMA weighting can compensate for the classic C/N_0 weighting.

Several groups of static GNSS data and one group of vehicle-borne kinematic GNSS data were processed by using the proposed 3DMA algorithm. In slight and medium urban environments, the proposed algorithm can accelerate some initial convergences and mitigate some outliers, but the positioning precision is not improved a lot and they are all with centimeter-level precision. For the static experiments in deep urban environments, it is difficult for classic PPP-RTK to achieve the positioning with a horizontal precision (< 20 cm) stably when only using elevation weighting. The unsatisfied performance owes to insufficient satellites, poor satellite geometries and complex contaminated GNSS measurements. In some experiments, less than 50% of the results are available. However, the proposed algorithm can improve the precision by more than 50%, and more than 90% of epochs could be available.

However, it is still a challenging problem to realize high-precision GNSS positioning in urban canyons. We will explore realizing the factor graph optimization algorithm in our future work to enhance the capacity of the weighting use and mitigate the effects of GNSS outlier measurements. In addition, more conditions in urban environments will be considered, like using the low-cost receiver, single-frequency data, etc.

Acknowledgements This study is funded by National Science Foundation of China (42025401) and Hubei Luojia Laboratory (No. 220100021). We thank IGS (International GNSS Service), Hong Kong Satellite Positioning Reference Station Network for the high-quality satellite products and the multi-GNSS data. The computation work was finished on the high-performance computing facility of Wuhan University. This research is supported by the University Grants Committee of Hong Kong under the scheme Research Impact Fund on the project R5009-21 "Reliable Multiagent Collaborative Global Navigation Satellite System Positioning for Intelligent Transportation Systems".

Author contributions JHG and LT devised the project and conceptual ideas. SX and LT worked out all technical details. SX developed the PPP-RTK algorithm and processed all data. GZ and HF provided technical supports about 3DMA and the experimental data. JG provided some satellite products and data. SX plotted the figures and wrote the draft of the paper. JHG and LT revised the paper. All authors approved of the manuscript.

Data availability The 3D building model data can be obtained at https://www.landsd.gov.hk/en/spatial-data/open-data.html. The GNSS data of the reference network can be obtained at https://www.geodetic.gov.hk/en/satref/satref.htm. The satellite products can be obtained at http://ftp.gipp.org.cn and ftp://ftp.gfz-potsdam.de. The GNSS data collected for experiments are available from the authors upon request.

Declarations

Conflict of interest The authors declare that they have no conflict of interest.

References

Ahmad KAB, Sahmoudi M, Macabiau C, Bourdeau A, Moura G (2013) Reliable GNSS positioning in mixed LOS/NLOS environments using a 3D model. In: European navigation conference (ENC), Vienne, Austria, Apr 2013, pp 1–9

Banville S, Collins P, Zhang W, Langley RB (2014) Global and regional ionospheric corrections for faster PPP convergence. Navigation 61(2):115–124

Boehm J, Niell A, Tregoning P, Schuh H (2006) Global mapping function (GMF): a new empirical mapping function based on numerical weather model data. Geophys Res Lett 33:L07304. https://doi.org/10.1029/2005GL025546

Counselman CC, Gourevitch SA (1981) Miniature interferometer terminals for earth surveying: ambiguity and multipath with Global Positioning System. IEEE Trans Geosci Remote Sens 19(4):244–252

Dong D, Bock Y (1989) Global positioning system network analysis with phase ambiguity resolution applied to crustal deformation studies in California. J Geophys Res 94(B4):3949–3966

Dong D, Wang M, Chen W et al (2016) Mitigation of multipath effect in GNSS short baseline positioning by the multipath hemispherical map. J Geod 90(3):255–262

Euler HJ, Goad C (1991) On optimal filtering of GPS dual frequency observations without using orbit information. Bull Geod 65:130–143

Franke R (1982) Scattered data interpolation: tests of some methods. Math Comput 38(157):181–200

Ge M, Gendt G, Rothacher MA, Shi C, Liu J (2008) Resolution of GPS carrier-phase ambiguities in precise point positioning (PPP) with daily observations. J Geod 82(7):389–399

Geng J, Meng X, Dodson AH, Ge M, Teferle FN (2010) Rapid re-convergences to ambiguity-fixed solutions in precise point positioning. J Geod 84(12):705–714

Geng J, Teferle FN, Meng X, Dodson AH (2011) Towards PPP-RTK: ambiguity resolution in real-time precise point positioning. Adv Space Res 47(10):1664–1673

Geng J, Chen X, Pan Y, Zhao Q (2019) A modified phase clock/bias model to improve PPP ambiguity resolution at Wuhan University. J Geod 93(10):2053–2067

Geng J, Guo J, Meng X, Gao K (2020) Speeding up PPP ambiguity resolution using triple-frequency GPS/BeiDou/Galileo/QZSS data. J Geod 94(1):6

Geng J, Wen Q, Zhang Q, Li G, Zhang K (2022) GNSS observable-specific phase biases for all-frequency PPP ambiguity resolution. J Geod 96:11. https://doi.org/10.1007/s00190-022-01602-3

Groves PD (2011) Shadow matching: a new GNSS positioning technique for urban canyons. J Navig 64(3):417–430

Groves PD, Jiang Z, Wang L, Ziebart MK (2012) Intelligent urban positioning using multi-constellation GNSS with 3D mapping and NLOS signal detection. In: Proceedings of ION GNSS 2012, Institute of Navigation, Nashville, TN, September, pp 458–472

Groves PD, Jiang Z, Rudi M, Strode P (2013) A portfolio approach to NLOS and multipath mitigation in dense urban areas. In: Proceedings of ION GNSS+ 2013, Institute of Navigation, Nashville, TN, September, pp 3231–3247

Groves PD, Jiang Z (2013) Height aiding, C/N_0 weighting and consistency checking for GNSS NLOS and multipath mitigation in urban areas. J Navig 66(5):653–669

Groves PD, Wang L, Adjrad M, Ellul C (2015) GNSS shadow matching: the challenges ahead. In: Proceedings of ION GNSS+ 2015, Tampa, Florida, Sept 2015, pp 2421–2443

Hsu L-T (2017) GNSS multipath detection using a machine learning approach. In: 2017 IEEE 20th international conference on intelligent transportation systems (ITSC), October 16–19, pp 1–6

Hsu L-T (2018) Analysis and modeling GPS NLOS effect in highly urbanized area. GPS Solut 22(1):7

Hsu L-T, Gu Y, Kamijo S (2015) NLOS correction/exclusion for GNSS measurement using RAIM and city building models. Sensors 15(7):17329–17349

Hsu L-T, Gu Y, Kamijo S (2016) 3D building model-based pedestrian positioning method using GPS/GLONASS/QZSS and its reliability calculation. GPS Solut 20(3):413–428

Icking L, Kersten T, Schön S (2020) Evaluating the urban trench model for improved GNSS positioning in urban areas. In: 2020 IEEE/ION position, location and navigation symposium (PLANS), pp 631–638

Jiang Z, Groves PD (2014) NLOS GPS signal detection using a dual-polarization antenna. GPS Solut 18(1):15–26

Langley RB (1999) Dilution of precision. GPS World 10(5):52–59

Lau L, Cross P (2007) Development and testing of a new ray-tracing approach to GNSS carrier-phase multipath modelling. J Geod 81(11):713–732

Lyard F, Lefevre F, Letellier T, Francis O (2006) Modelling the global ocean tides: modern insights from FES2004. Ocean Dyn 56(5):394–415

Miura S, Hsu LT, Chen F, Kamijo S (2015) GPS error correction with pseudorange evaluation using three-dimensional maps. IEEE Trans Transp Syst 16(6):3104–3115

Myers L, Sirois MJ (2006) Spearman correlation coefficients, differences between. Encycl Stat Sci 12

Ng HF, Hsu L-T (2021) 3D mapping database-aided GNSS RTK and its assessments in urban canyons. IEEE Trans Aerosp Electron Syst 57(5):3150–3166

Ng HF, Zhang G, Hsu L-T (2019) GNSS NLOS pseudorange correction based on skymask for smartphone applications. In: Proceedings of ION GNSS+ 2019, Miami, Florida, September 2019, pp 109–119

Ng HF, Zhang G, Yang KY, Yang SX, Hsu LT (2020a) Improved weighting scheme using consumer-level GNSS L5/E5a/B2a pseudorange measurements in the urban area. Adv Space Res 66(7):1647–1658

Ng HF, Zhang G, Hsu L-T (2020b) A computation effective range-based 3D mapping aided GNSS with NLOS correction method. J Navig 73(6):1202–1222

Odijk D, Zhang B, Khodabandeh A, Odolinski R, Teunissen PJG (2016) On the estimability of parameters in undifferenced, uncombined GNSS network and PPP-RTK user models by means of S-system theory. J Geod 90(1):15–44

Petit G, Luzum B, (eds.) (2010) IERS Conventions (2010), IERS Technical Note 36, Verlagdes Bundesamts für Kartographie und Geodäsie, Frankfurt am Main, Germany

Peyraud S, Bétaille D, Renault S, Ortiz M, Mougel F, Meizel D, Peyret F (2013) About non-line-of-sight satellite detection and exclusion in a 3D map-aided localization algorithm. Sensors 13(1):829–847

Psychas D, Verhagen S (2020) Real-time PPP-RTK performance analysis using ionospheric corrections from multi-scale network configurations. Sensors 20(11):3012

Ragheb AE, Clarke PJ, Edwards SJ (2007) GPS sidereal filtering: coordinate-and carrier-phase-level strategies. J Geod 81(5):325–335

Realini E, Reguzzoni M (2013) goGPS: open source software for enhancing the accuracy of low-cost receivers by single-frequency relative kinematic positioning. Meas Sci Technol 24(11):115010

Rizos C (2002) Network RTK research and implementation—a geodetic perspective. J GPS 2(1):144–150

Saastamoinen J (1972) Contributions to the theory of atmospheric refraction. Bull Geod 105:279–298

Schaer S, Villiger A, Arnold D, Dach R, Prange L, Jäggi A (2021) The CODE ambiguity-fixed clock and phase bias analysis products: generation, properties, and performance. J Geod 95(7):1–25

Suzuki T, Kubo N (2013) Correcting GNSS multipath errors using a 3D surface model and particle filter. In: Proceedings ION GNSS+ 2013, Institute of Navigation, Nashville, TN, September 16–20, pp 1583–1595

Teunissen PJG, De Jonge PJ, Tiberius CCJM (1997) The least-squares ambiguity decorrelation adjustment: its performance on short GPS baselines and short observation spans. J Geod 71(10):589–602

Teunissen PJG, Odijk D, Zhang B (2010) PPP-RTK: results of CORS network-based PPP with integer ambiguity resolution. J Aeronaut Astronaut Aviat Ser A 42(4):223–230

van Diggelen F (2021) End game for urban GNSS: Google's use of 3D building models. Inside GNSS 16(2)

Wen W, Zhou Y, Zhang G, Fahandezh-Saadi S, Bai X, Zhan W, Hsu L-T (2020) Urbanloco: a full sensor suite dataset for mapping and localization in urban scenes. In: 2020 IEEE international conference on robotics and automation (ICRA), pp 2310–2316

Won DH, Ahn J, Lee SW et al (2012) Weighted DOP with consideration on elevation-dependent range errors of GNSS satellites. IEEE Trans Instrum Meas 61(12):3241–3250

Wu G, Chen J, Wu X, Hu J (2020) Modeling and assessment of regional atmospheric corrections based on undifferenced and uncombined PPP-RTK. Acta Geodaetica Et Cartographica Sinica 49(11):1407–1418

Wübbena G, Schmitz M, Bagge A (2005) PPP-RTK: precise point positioning using state-space representation in RTK networks. In: Proceedings of ION GNSS 18th international technical meeting of the satellite division, Long Beach, US, pp 2584–2594

Zhang B, Teunissen PJG, Odijk D (2011) A novel un-differenced PPP-RTK concept. J Navig 64(S1):S180–S191

Zhang G, Wen W, Hsu L-T (2018) A novel GNSS based V2V cooperative localization to exclude multipath effect using consistency checks. In: 2018 IEEE/ION position, location and navigation symposium (PLANS), pp 1465–1472

Zhang B, Chen Y, Yuan Y (2019) PPP-RTK based on undifferenced and uncombined observations: theoretical and practical aspects. J Geod 93(7):1011–1024

Zhong Q, Groves PD (2021) Multi-epoch 3D-mapping-aided positioning using bayesian filtering techniques. In: Proceedings of ION GNSS+ 2021, St. Louis, Missouri, Sept 2021, pp 195–225

Zumberge JF, Heflin MB, Jefferson DC, Watkins MM, Webb FH (1997) Precise point positioning for the efficient and robust analysis of GPS data from large networks. J Geophys Res 102(B3):5005–5017